A Comparison of Optic Nerve Head Morphology Viewed by Spectral Domain Optical Coherence Tomography and by Serial Histology

Nicholas G. Strouthidis,[1] *Jonathan Grimm,*[1] *Galen A. Williams,*[1] *Grant A. Cull,*[1] *David J. Wilson,*[2] *and Claude F. Burgoyne*[1]

PURPOSE. To compare serial optic nerve head (ONH) histology with interpolated B-scans generated from a three-dimensional (3-D) spectral domain (SD)-OCT ONH volume acquired in vivo from the same normal monkey eye.

METHODS. A 15° ONH SD-OCT volume was acquired in a normal monkey eye, with IOP manometrically controlled at 10 mm Hg. After perfusion fixation at 10 mm Hg, the ONH was trephined, the specimen embedded in a paraffin block, and serial sagittal sections cut at 4-μm intervals. The location of each histologic section was identified within the optic disc photograph by matching the position of the retinal vessels and of Bruch's membrane opening. By altering the angles of rotation and incidence, interpolated B-scans matching the location of the histologic sections were generated with custom software. Structures identified in the histologic sections were compared with signals identified in the matched B-scans.

RESULTS. Close matches between histologic sections and interpolated B-scans were identified throughout the extent of the ONH. SD-OCT identified the neural canal opening as the termination of the Bruch's membrane–retinal pigment complex and border tissue as the innermost termination of the choroidal signal. The anterior lamina cribrosa and its continuity with the prelaminar glial columns were also detected by SD-OCT.

CONCLUSIONS. Volumetric SD-OCT imaging of the ONH generates interpolated B-scans that accurately match serial histologic sections. SD-OCT captures the anterior laminar surface, which is likely to be a key structure in the detection of early ONH damage in ocular hypertension and glaucoma. (*Invest Ophthalmol Vis Sci.* 2010;51:1464–1474) DOI:10.1167/iovs.09-3984

The application of optical coherence tomography (OCT) technology in clinical glaucoma practice has largely centered on imaging the peripapillary retinal nerve fiber layer. This approach has shown promise in assisting the clinician in both diagnosing glaucoma and detecting disease progression.[1–6] There is mounting evidence to suggest that the primary site of injury to the retinal ganglion cell axon is at the level of the lamina cribrosa.[7–12] An ability to image the lamina cribrosa and other structures deep within the optic nerve head (ONH) would therefore constitute a major advance. Indeed, recent work using postmortem three-dimensional (3-D) histomorphometric ONH reconstructions has identified several cardinal morphologic changes at the earliest stage of experimental glaucoma.[13–16] These changes include a thickening of the prelaminar tissue (as distinct from the thinning one would expect to observe at the later stages of the neuropathy), posterior deformation and thickening of the lamina cribrosa, and expansion of the scleral canal. We propose that the identification of these changes in vivo would help to identify those eyes with the earliest signs of distress in response to an IOP-mediated insult and, as such, at high risk of future functional damage.

The ability of OCT to image retinal morphology has been validated by several seminal studies in which investigators have sought to compare OCT tomograms to conventional serial histology in humans,[17,18] nonhuman primates,[19–21] tree shrews,[22] rodents,[23] and pigs.[24] Although not the principal goal, several of these studies also included brief comments pertaining to ONH and peripapillary retinal morphology.[21,22,24] Besides these commentaries, there have not been, to date, any formal, rigorous comparisons of ONH morphology as imaged by OCT and by light microscopy. An obvious reason for this is the insufficiency of the axial (depth) resolution of conventional time domain OCT ($\sim$10 μm) for resolving structures deep under the surface of the optic disc cup. With the commercial introduction of spectral domain (SD)-OCT, which has both an improved axial resolution (approaching 5 μm) and vastly increased acquisition speed, the 3-D detection of deep ONH targets has become tangible.

Several recent reports suggest that SD-OCT imaging of the human ONH can capture the lamina cribrosa.[25,26] Although these reports are encouraging, it is essential that the SD-OCT's ability to capture deep ONH targets be validated by comparison with conventional serial histology. The purpose of this study was to compare interpolated SD-OCT B-scans generated from a volumetric SD-OCT reconstruction acquired in vivo from a normal monkey ONH with serial histologic sections obtained postmortem from the same ONH. This study required the development of a novel method of generating tailor-made interpolated B-scans at any orientation from the 3-D SD-OCT volume. This method is fully described.

METHODS

ONH Imaging

The study was performed on the left eye of a 6.8-year-old, 4.5-kg female rhesus macaque (*Macaca mulatta*). The local Institutional Animal Care
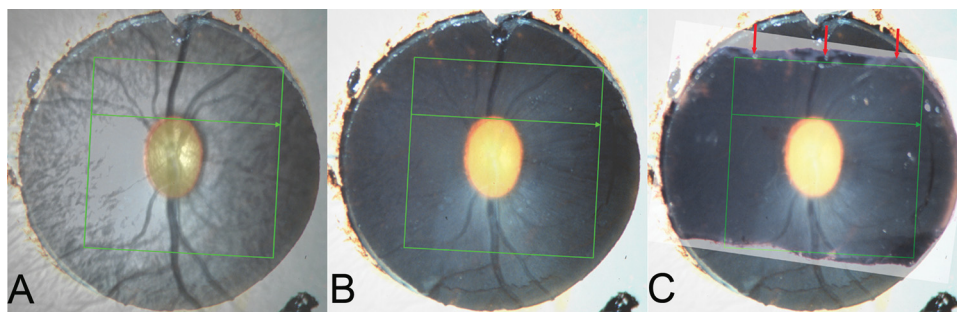
FIGURE 1. Trephining the ONH in the orientation of the acquired B-scan. (**A**) The SD-OCT IR image including the 15° acquisition box, viewed at 50% opacity, was aligned to an image of the ONH specimen. (**B**) The coordinates of the acquisition box were burned onto the image. (**C**) Cuts were made in the specimen, in an attempt to get the closest approximation to the orientation of the acquired B-scans. The cut made in the superior part of the specimen (*red arrows*) most closely matched the acquired B-scan orientation. The specimen was embedded with the superior cut surface facing downward.

and Use Committee (Legacy Health System, Portland, OR) approved the study, and the subject animal was treated in accordance with the ARVO Statement for the Use of Animals in Ophthalmic and Vision Research.

In vivo imaging with a rigid plano contact lens placed onto the corneal surface was performed immediately before the animal was killed. The monkey was anesthetized with ketamine and isoflurane, and the pupil was dilated with 1 drop each of 1% tropicamide, 2.5% phenylephrine hydrochloride, and 2% cyclopentolate hydrochloride. The intraocular pressure (IOP) was adjusted to 10 mm Hg with a manometer connected to a 27-gauge cannula, which was inserted into the temporal anterior chamber. After IOP of 10 mm Hg was maintained for 30 minutes, an experienced technician (GAW) acquired a pair of left optic disc stereophotographs with a simultaneous stereo fundus camera (TRC-WT Retinal Camera; Topcon, Paramus, NJ).

SD-OCT imaging of the left ONH was performed with a commercially available device (Spectralis; Heidelberg Engineering, Heidelberg, Germany). For the purposes of this study, a horizontal raster scan pattern was acquired with 290 individual horizontal B-scans, 768 A-scans per B-scan, and each B-scan acquired nine times and averaged for speckle noise reduction. The scan was centered on the ONH, with a 15° retinal window. The device's built-in eye-tracking facility was turned on during acquisition. The native viewing software automatically registered all consecutive B-scans relative to one another in the *z*-axis.

Perfusion Fixation

At the conclusion of imaging, the animal was killed by perfusion fixation through the descending aorta with 1 L of 4% buffered hypertonic paraformaldehyde solution followed by 6 L of 5% buffered hypertonic glutaraldehyde solution. IOP was maintained at 10 mm Hg for 1 hour, after which the left orbital contents were exenterated via a lateral orbitotomy. All orbital tissue was immediately removed from the globe. The anterior chamber was removed 2 to 3 mm posterior to the limbus, and the posterior scleral shell with intact optic nerve, ONH, choroid, and retina was placed in 5% glutaraldehyde for storage.

Tissue Preparation

The optic nerve was removed leaving a 3-mm stump attached to the globe. The ONH and peripapillary sclera were trephined (6 mm in diameter, passed from the vitreous surface through the sclera), and a triangular notch was cut into the superior peripapillary sclera. The trephined specimen was photographed at ×2 magnification with a single-lens reflex (SLR) camera (FM2; Nikon, Tokyo, Japan) attached to a dissecting microscope (Stereomaster; Thermo Fisher Scientific, Inc., Waltham, MA).

Co-localization of the SD-OCT Infra-Red Image with the Trephined ONH Image

The location of the 15° SD-OCT acquisition window was overlaid onto the digital image of the trephined ONH specimen to generate histologic sections at approximately the same orientation as the acquired SD-OCT B-scans (Fig. 1). First, the 35-mm color slide image of the specimen was digitized at a resolution of 4800 dpi with a color-calibrated scanner (ArtixScan M1 Slide Scanner; Microtek Laboratory, Inc., Fontana, CA). Commercially available image-processing software (Adobe Photoshop CS3, Adobe Systems, Inc., San Jose, CA) was used to overlay the SD-OCT infra-red (IR) image onto the digitized ONH image, by matching the central retinal vessels and their bifurcations. Figure 1A shows the co-localized IR image, including the SD-OCT acquisition box, at 50% opacity, superimposed onto the ONH photograph. The co-ordinates of the SD-OCT acquisition box were burned onto the image of the ONH specimen (Fig. 1B).

Tissue Embedding

Three attempts were made to cut the inferior edge of the specimen under the dissecting microscope parallel to the inferior boundary of the co-localized acquisition box. The cuts were made with a single-edged, number 12 industrial razor blade (VWR, West Chester, PA), with the image shown in Figure 1B used as a reference. After each cut, the ONH specimen was rephotographed, and the resultant digital image was co-localized to Figure 1B so as to assess the accuracy of the cut relative to the inferior border of the superimposed acquisition box. After each inferior cut was found to be inaccurate, two additional cuts were made on the superior edge of the specimen, the second of which best approximated the desired orientation (Fig. 1C). The specimen was then embedded in paraffin by using a standard histologic technique, with the superior cut surface facing downward in the block.

Histologic Sectioning and Staining

The ONH specimen block was sectioned at 4-μm intervals with a microtome (RM 2155; Leica Biosystems, St. Louis, MO). The sections were floated in a water bath (56°C) and picked up onto slides that were incubated overnight at 60°C. Before staining, the slides were deparaffinized through two changes of xylene for 5 minutes. The slides were then hydrated through two changes each of absolute alcohol and 95% alcohol followed by one change of 70% alcohol and then a rinse in running tap water.

Every fourth section (16-μm intervals) was stained with hematoxylin and eosin (HE) by immersion for 4 minutes in Shandon's instant hematoxylin (Thermo-Fisher Scientific, Inc.), rinsed in running tap water for 5 minutes, counterstained for 45 seconds in eosin, dehydrated, and mounted in a synthetic medium (Eukitt; Sigma-Aldrich, St. Louis, MO).
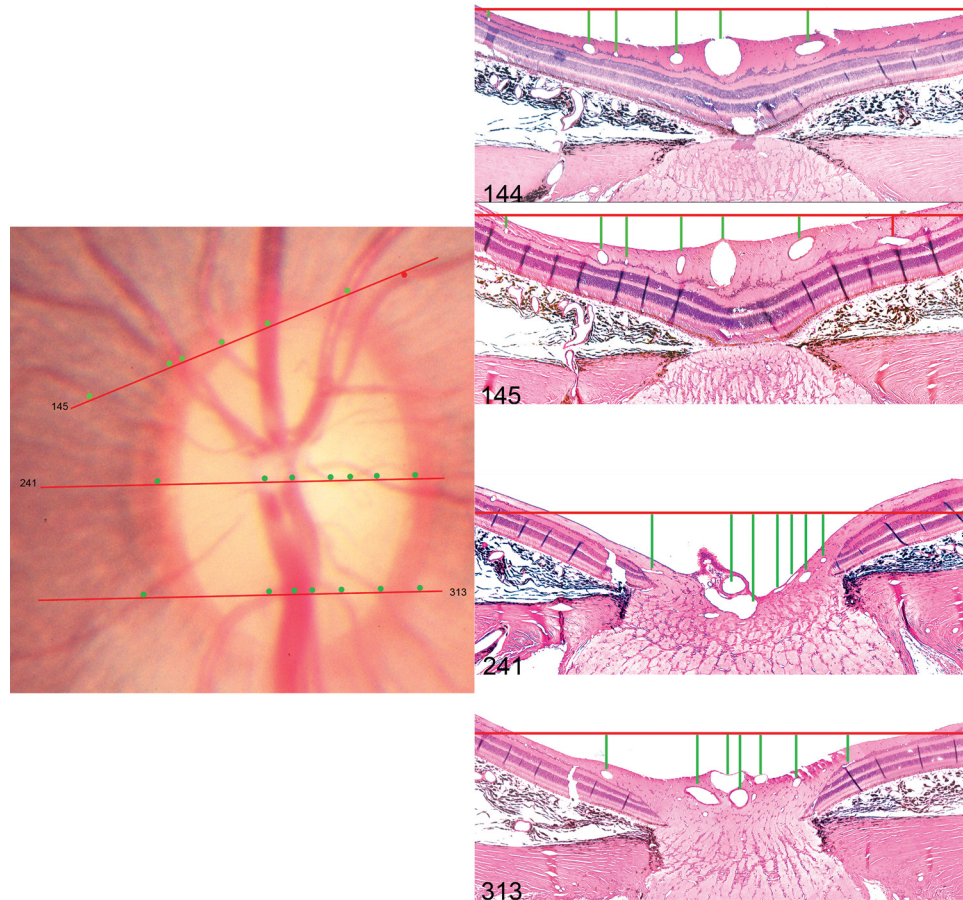
FIGURE 2. Method of orienting histologic sections to the disc photograph. The topographic locations of histologic sections 145, 241, and 313 are shown. The orientation of each section (*red lines* in the disc photograph) is judged by assessing the relative spacing of the retinal vessels, marked by *circular glyphs* in the disc photograph and by *vertical lines* in the histologic sections. The temporal vessel outlined by a *red glyph* is absent in section 144, but appears in the next section (145). The superior opening in Bruch's membrane (superior disc margin) was near section 145 (described in detail in Fig. 5) and the inferior opening in Bruch's membrane was near section 335 (not shown in this figure, but described in detail in Fig. 6) Hematoxylin and eosin; magnification, ×10.

In addition to the HE-stained slides, individual unstained slides from regions of interest within the ONH were selected for alternative staining (all stains acquired from Thermo-Fisher Scientific, Inc.). For Masson trichrome (MT) staining, the deparaffinized, hydrated slides were immersed in Weigert's hematoxylin for 10 minutes and rinsed in running water for 10 minutes. They were then immersed in Biebrich scarlet-acid fuchsin for 5 minutes and rinsed in distilled water. Finally, they were immersed in phosphomolybdic-phosphotungstic acid solution for 10 minutes and aniline blue solution for 3 minutes. They were rinsed in distilled water, immersed in 1% glacial acetic acid, dehydrated, cleared, and mounted. Burke's modification for the combined staining of cells and fibers in the nervous system was used to achieve luxol fast blue/cresyl violet acetate (LFB) staining.[27] Finally, staining with a 1:1 (vol/vol) mixture of Ponceau-saffron and acid fuchsin was performed on a few selected slides, as this is the connective tissue stain used in our 3-D histomorphometric reconstruction technique.[12,15,16]

Slides selected for comparison with SD-OCT B-scans were imaged at 10× magnification with an inverted microscope (DM IRBE; Leica) and image capture software (Life Science, ver. 8.10.20, Bioquant Image Analysis Corp., Nashville, TN).

Orientation of Histologic Sections Relative to the Optic Disc Photograph

The 35-mm color stereo slide pair was digitized as outlined for the photograph of the trephined specimen (Fig. 2). The HE-stained sections (every fourth section) were then reviewed to identify in which slides the superior and inferior openings in the retinal pigment epithelium (RPE) and Bruch's membrane were present. These slides therefore served as cardinal orientation slides, corresponding to the superior and inferior disc margins on the clinical disc photograph.[28] The angle of rotation at which each section was acquired was ascertained by tracking the location of each major retinal vessel and its spacing relative to other vessels and relative to the boundaries of the optic nerve and then referencing to a location on the clinical photograph consistent with these anatomic relationships. The clinical location of each histologic section was marked on the disc photograph, which was then co-localized and aligned to the en face SD-OCT image by using the same method.

Generation of Interpolated B-Scans for Comparison with Serial Histology

Having taken steps to ensure a close match between the histologic sections and the acquired SD-OCT B-scans, we then attempted to fine tune the accuracy of the match by correcting for two sources of discrepancy (Fig. 3). First, we corrected for the degree by which the angle of rotation of the histologic section differed from that of the acquired B-scan. Second, we corrected for the degree by which the angle of incidence of the microtome blade and the angle of incident light from the SD-OCT device might differ. To do so, we developed a method of extracting interpolated B-scans, at any angle of rotation and
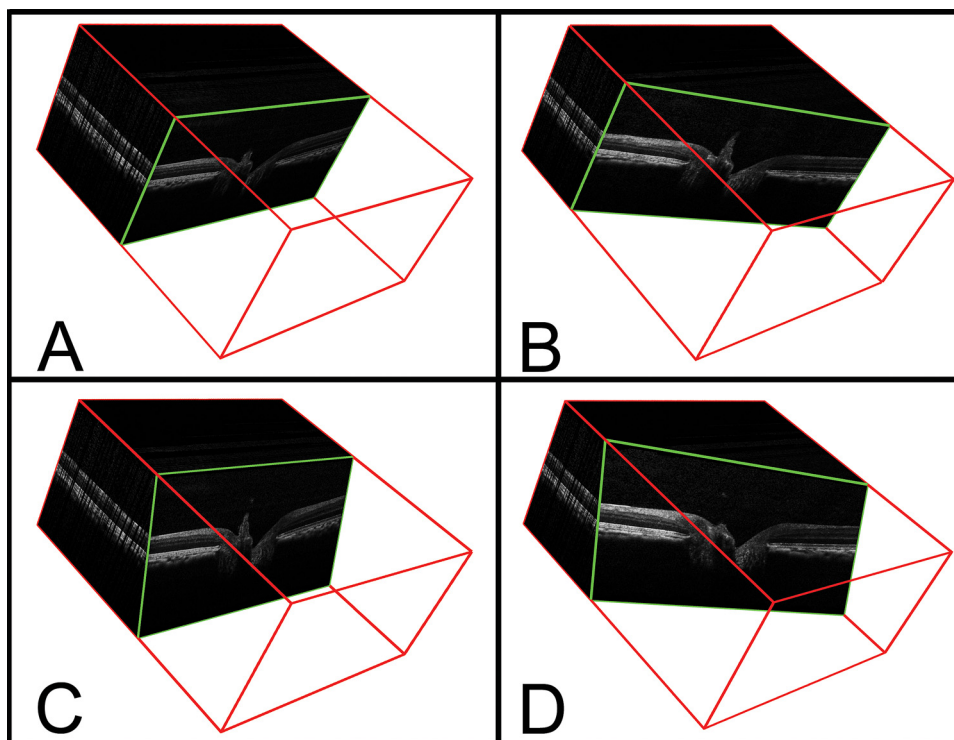
Figure 3. Method of identifying interpolated B-scans from the SD-OCT volumetric reconstruction. (**A**) A representative acquired B-scan is shown within the 3-D volume (enclosed within a *red cube*) generated from a 290 × 768 horizontal raster scan. The angle of rotation of the B-scan was 90° and the angle of incidence was 0°. (**B**) The interpolated B-scan shown was generated in a 20° clockwise rotation (angle of rotation, 70°); the angle of incidence was unchanged. (**C**) The interpolated B-scan shown was generated after a −20° change in the angle of incidence. (**D**) The interpolated B-scan shown was generated with an angle of rotation of 70° and an angle of incidence of −20°.

incidence, from the data contained within the 3-D ONH SD-OCT volume (Fig. 3).

Custom software (based on the Visualization Toolkit; VTK, Clifton Park, NY), was used to generate a B-scan plane (*x–z* plane) and to rotate it about the *z*-axis to reproduce the en face angle of rotation. The B-scan plane was then rotated about the *x*-axis to reproduce the angle of incidence. These manipulations were translated to a specified point within the 3-D SD-OCT volume onto which a fine grid of 1×1-μm squares was overlaid. The application of this fine grid onto the B-scan plane was designed to overcome the distortion from the misalignment of the plane with the volume occurring at the subpixel level. The fine-grid squares were used to sample the volume by a nearest neighbor technique, wherein the distance of the centroid of the square in the plane to the centroids of the pixels in the volume was computed, and the value from the pixel in the volume with the shortest centroid-to-centroid distance was selected. These data were saved as a floating point TIFF image, and the plane was shifted along its normal until a complete family of interpolated B-scans was generated. This software could alter the angle of rotation and incidence by 0.5° increments.

The method by which the interpolated B-scan angle of rotation was decided for each histologic section is illustrated in Figure 4. The disc photograph, containing the topographical location of the HE-stained sections (Fig. 4A) was co-localized to the en face SD-OCT image, as described earlier. With a fixed center of rotation, the angle of rotation of each histologic section was calculated with reference to the horizontal raster acquisition box, in which the vertical axis is 0° and the horizontal axis is 90°. With the angle of rotation identified, we used the purpose-built software to generate a complete series of interpolated B-scans for that angle, as though the acquisition window had shifted to the selected angle of orientation.

Once the optimum angles of rotation had been identified, the angle of incidence was estimated. The interpolated B-scans generated with an angle of incidence of 0° (perpendicular to the imaged surface) were compared to the histologic sections from the same topographic locations. The angle of incidence was then varied by 0.5° increments until the interpolated B-scans best matched the histologic section at each location. An example demonstrating the effect of varying the angle of incidence is shown in Figure 5.

Comparison of Histologic Sections to Matched Interpolated B-Scans

Matched interpolated B-scans (defined to be best corrected for angle of rotation and incidence) and their histologic sections were then qualitatively compared, to identify which structures within the ONH could be identified by SD-OCT. To facilitate this, we attempted to align the ONH structures within each B-scan with their respective locations within the matched histologic section. Alignment was performed with image-processing software (Photoshop CS3; Adobe Systems, Inc.). Rotation and scaling in a 1:1 ratio were performed. We did not warp or morph images to correct for tissue-processing artifacts in the histologic sections, such as differential horizontal or vertical shrinkage, choroidal expansion, and retinal elevation.

RESULTS

Topographic Location of Histologic Sections

Histologic sections ($n = 525$), with a minimum separation of 4 μm between each section, were generated from the trephined ONH sections. Figure 4A illustrates the location of the initial HE-stained sections (every fourth section) throughout the full extent of the disc photograph. HE-stained sections in which
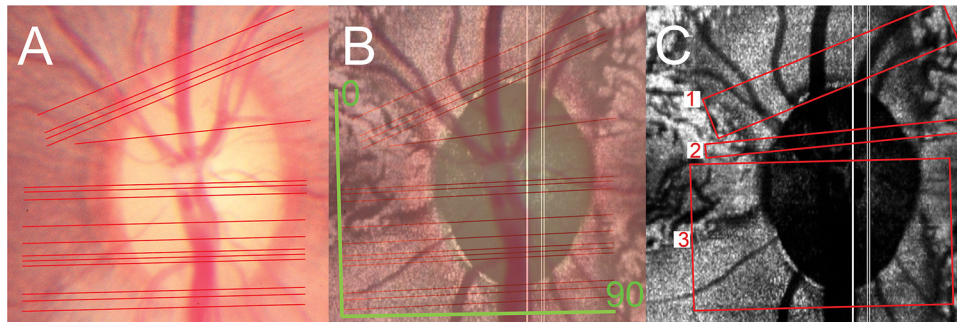
FIGURE 4. Method of identifying the B-scan angle of rotation. (A) The topographic orientation of serial hematoxylin and eosin–stained sections is depicted as a series of *red lines* in the disc photograph. There was a minimum separation of 16 μm between sections. Sections that could not be oriented because of poorly preserved retina account for the variable width of gaps between the lines. (B) The image shown (A, viewed at 50% opacity) was colocalized to the en face SD-OCT image (C-scan). *Green lines*: 0° and 90° orientations of the actual acquired horizontal raster B-scans. (C) The angle of rotation of the histologic sections assessed relative to that of the acquired B-scans varied within three regions: 73.5° in histologic sections from region 1, 87° in sections from region 2, and 89° in sections from region 3.

the retina was insufficiently preserved to allow the accurate identification of retinal vessels were not used for comparison.

Generation of Matched Interpolated B-Scans

Histologic sections in the superior part of the nerve (Fig. 4C; region 1) required interpolated SD-OCT B-scans to be generated at an angle of rotation of 73.5°. Inferior to this, there was a small portion of the nerve (Fig. 4C; region 2) in which the matched angle of rotation was 87°. The remaining sections (Fig. 4C; region 3) required an angle of 89°, which was almost identical with the acquired B-scan angle of 90°.

The effect of altering the angle of incidence of the interpolated B-scan for a given histologic section is illustrated in Figure 5 for section 145, which was located close to the superior disc margin. In this section, the retinal pigment epithelium (RPE) and Bruch's membrane were still intact, although there was an opening in both the choroid and the sclera. An interpolated B-scan generated at an angle of incidence of 0°, perpendicular to the retinal surface, (Fig. 5B) was not as accurate as the one generated at an angle of incidence of −18°, which was angled toward the nerve (Fig. 5C).

Figure 6A shows histologic section 335, which is located close to the inferior disc margin. In this section, an opening in the choroidal space is present below the intact RPE. A very small portion of the optic nerve is visible above a small, intact portion of peripapillary sclera, suggesting that the section was acquired at a less oblique angle than was section 145. Figure 6B shows the matched interpolated B-scan, generated at an angle of incidence of 0°. All the major vessels in the histologic section are detectable in this interpolated B-scan. Likewise, the opening in the choroid is present, along with a faintly continuous RPE/Bruch's membrane complex signal. It should be noted that the shadow cast by the presence of two large retinal vessels above this region would have contributed to the faintness of the latter signal. The sclera is not detected in this section, although there is a faint signal below the choroidal opening, suggesting that some reflected light from the underlying optic nerve has been captured.

An angle of incidence of −18° was found to achieve the best matches in the part of the nerve where sections were acquired at an angle of rotation of 73.5° (Fig. 4C, region 1). Where the angle of rotation was 87° (Fig. 4C, region 2), an angle of incidence of −10° achieved the best matches. In the remainder of the ONH, where the angle of rotation was 89° (Fig. 4C, region 3), the best matches were achieved with an angle of incidence of 0°.

Detection of Deep ONH Structures

Two examiners (NGS, CFB) qualitatively compared the matches between interpolated B-scans and the respective histologic sections. The vitreal surface of the ONH was detectable by SD-OCT throughout its full extent. However, SD-OCT visualization of structures deep to the surface was poor in regions where shadows were cast by the central retinal vessels.

Interpolated B-scans matched to histologic sections acquired from the central part of the disc (sections 256–260) were selected for the detailed assessment of deep ONH imaging, as they had the largest continuous shadow-free areas on either side of the central retinal vessels (Figs. 7, 8, 9). For these comparisons, the same interpolated B-scan was matched to each section, because the separation between adjacent B-scans was approximately 12 to 16 μm, which was comparable to the separation between the selected histologic sections. Within these sections, a prominent Bergmeister's papilla was clearly visualized within both the histologic sections and the interpolated SD-OCT B-scan.

Neural Canal Opening. We have previously described the neural canal to be the passage through which retinal ganglion cell axons traverse the wall of the eye, beginning at the plane of the RPE/Bruch's membrane complex (the neural canal opening, NCO) and continuing through the choroidal and scleral portions of the canal.[28,29] Figure 7 demonstrates the SD-OCT detected features of the NCO, as compared to their underlying histologic basis. The RPE/Bruch's membrane complex was defined to be the posterior signal from the hyperreflective triple stripe below the dark, hyporeflective outer nuclear layer.[29,30] We defined the innermost termination of this signal at either side of the neural canal as the NCO.[29] In Figure 7A, section 257 (HE-stained) is shown, with the temporal canal opening magnified in the inset. The retinal layers can be seen to taper downward toward a point between the outer nuclear and photoreceptor layers (marked by black arrows). In this section, the termination of the RPE was external to the termination of Bruch's membrane, and these same relationships were easily discerned within the matched interpolated B-scan (Fig. 7B). Within section 260 (Fig. 7C), Ponceau S stain better revealed the extension of unpigmented Bruch's membrane beyond the RPE.

Border Tissue of Elschnig. The border tissue is a flange or strut of connective tissue arising from the sclera to meet Bruch's membrane and, in doing so, acting as the junction between the innermost termination of the choroid and the adjacent retinal ganglion cell axon bundles. In Figure 8A (histologic section 258,
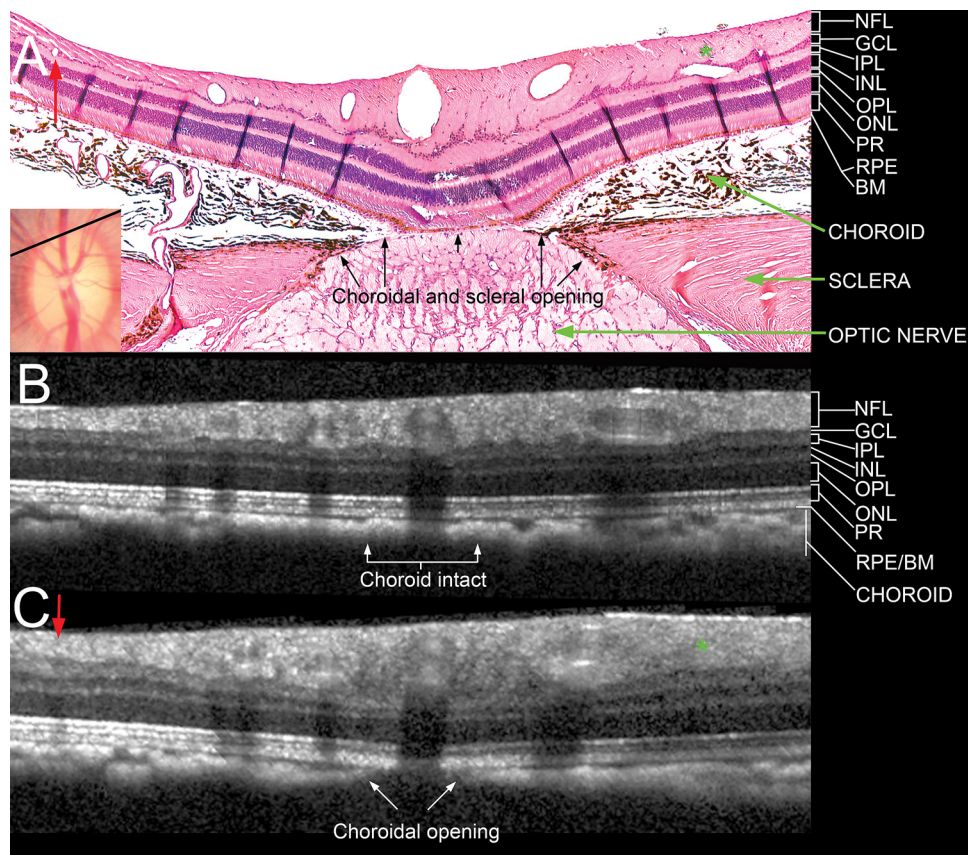
Figure 5. Comparison of a histologic section located near the superior Bruch's membrane opening (disc margin) with matched interpolated B-scans. (**A**) Section 145, with its topographical location shown as a *black line* in the disc photograph (*inset*, also shown in Fig. 2). Note the presence of a small vessel in the nasal (*left*) part of the section (*red arrow*) and an oblique vessel in the temporal (*right*) part of the section (*green asterisk*). There was an opening in the choroid and sclera, but the RPE and Bruch's membrane were intact over the optic nerve. (**B**) An interpolated section generated from the same topographic location, at an angle of rotation of 73.5°, but with an angle of incidence of 0° (perpendicular to the surface). Neither of the vessels highlighted in (**A**) was detected, and the choroidal signal appeared to be continuous. (**C**) An interpolated B-scan generated from the same location as (**B**), but with an angle of incidence of −18° (angled toward the nerve). The two vessels became visible in the correct location (labeled with a *red arrow* and a *green asterisk*). An opening in the choroid was visible, the RPE/BM complex remained intact, but no signal from the deeper optic nerve and lamina cribrosa was detected. NFL, nerve fiber layer; GCL, ganglion cell layer; IPL, inner plexiform layer; INL, inner nuclear layer; OPL, outer plexiform layer; ONL, outer nuclear layer; PR, photoreceptor layer; RPE/BM, retinal pigment epithelium/Bruch's membrane complex. Hematoxylin and eosin; magnification, ×10.

stained with MT), the border tissue of Elschnig is seen at either side of the neural canal, between the sclera and Bruch's membrane. Within the matched interpolated B-scan (Fig. 8B), the border tissue corresponds to the junction of the choroidal signal with the nerve and the heavy pigment located just below it, at the edge of the sclera. Within this matched interpolated B-scan, the anterior scleral surface is not visible.

Prelaminar Glial Columns and the Anterior Lamina Surface. The prelaminar glial columns are most easily visualized in the HE-stained section (Fig. 9A, red arrows; section 257) where the glial nuclei are prominently stained; to a lesser extent, the connective tissue component of these columns is detectable with MT staining (Fig. 9B; section 258). These columns can be seen to commence within the neural canal at approximately the level of the NCO and the border tissue. The columns extend posteriorly as vertical struts until the point where they merge with the more horizontally oriented laminar beams. Vertically oriented striations within the matched interpolated B-scan (Fig. 9A) appear to correspond to the prelaminar glial columns.

In Figure 9B, we define the anterior laminar surface in the histologic section to be the innermost point at which horizontally/transversely oriented connective tissue can be identified. Within the matched interpolated B-scan there appears to be a distinction between the prelaminar glial columns (vertical striations) and the anterior laminar surface (transversely oriented signal), particularly in the nasal side of the scan. Although the precise peripheral scleral insertion of the lamina cannot be visualized in this B-scan, the anterior laminar surface signal can be seen to bend upward toward a point below the border tissue on both sides of the neural canal. The posterior laminar surface (Fig. 9C) is not detectable in the matched interpolated B-scan.

Discussion

This study represents an important step in verifying the deep ONH imaging capabilities of SD-OCT. The following ONH targets could be identified by SD-OCT: the vitreal surface of the
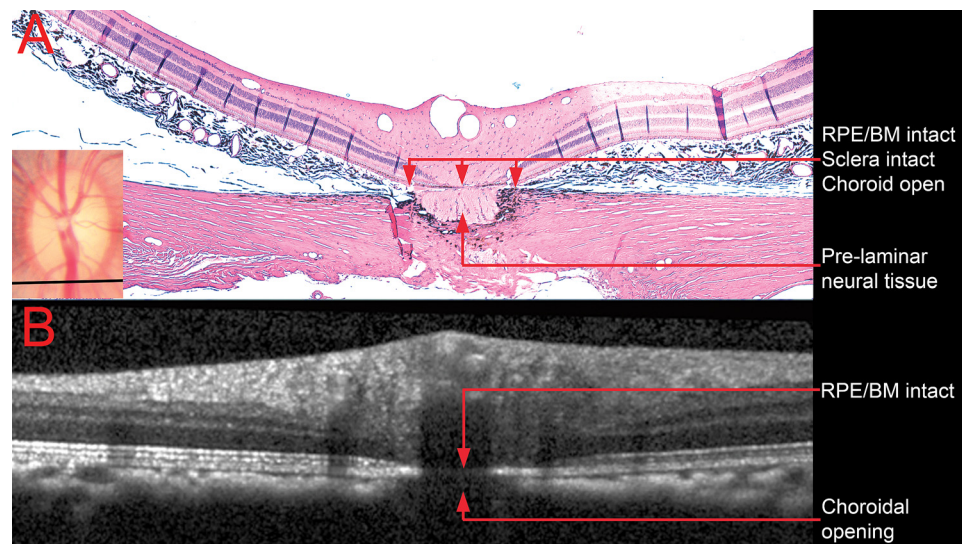
FIGURE 6. Comparison of a histologic section located near the inferior Bruch's membrane opening (disc margin) with its matched interpolated B-scan. (**A**) Section 335 is shown with its topographical location depicted (*black line*) in the clinical photograph (*inset*). (**B**) The matched interpolated B-scan was acquired at an angle of rotation of 89°, but the angle of incidence was kept at 0°. The retinal pigment epithelium/Bruch's membrane complex was intact, but the opening in the choroid was present, as in the histologic section. The prelaminar neural tissue and the intact sclera were most likely not detected because of shadowing from the central retinal vessels. Hematoxylin and eosin; magnification, ×10.

ONH, prelaminar tissue, NCO, border tissue, choroid, prelaminar glial columns, and the anterior laminar surface. The anterior and posterior scleral surfaces, the peripheral insertion of the lamina, and the posterior laminar surface were not detectable within this SD-OCT volume.

In a series of recent articles, we identified the NCO as a relatively planar, continuous structure that underpins the disc margin in most monkey eyes.[28,29] For these reasons, and the likelihood that an automated segmentation algorithm will reliably detect the NCO, we have proposed the NCO as a suitable basis for an SD-OCT reference plane.[29] In the present study, we were unable to identify a distinct signal from Bruch's membrane separate from the RPE. Of interest, it appears that the SD-OCT-defined NCO (Fig. 7B, magnified inset) took into account a portion of unpigmented Bruch's membrane, extending beyond the termination of the retinal pigment epithelium (Fig. 7C, magnified inset). However, in this particular SD-OCT volume, a transition point, such as an abrupt decrease in the width of the RPE/Bruch's membrane complex, was not detected.

The detection of an SD-OCT signal attributable to the border tissue has clinical relevance in terms of defining the optic disc margin. We have recently determined, using postmortem 3-D histomorphometric reconstructions, that the underlying disc margin anatomy in the monkey eye is governed by the orientation of border tissue relative to Bruch's membrane.[28] We identified two principal border tissue orientations. Internally, oblique border tissue occurs where it extends from the sclera toward the neural canal to meet Bruch's membrane (the most common orientation). Externally oblique border tissue occurs where it extends from the sclera, away from the neural canal, to meet Bruch's membrane. This orientation, when present, is located in the temporal half of the disc. In their classic description of the ultrastructure of the human and monkey ONH, Anderson and Hoyt[31] were unable to detect border tissue of Elschnig in the monkey eye. A connective tissue strut emanating from the scleral surface is clearly visible in the MT-stained section (Fig. 8A, white arrows). This structure almost certainly represents border tissue of Elschnig, although it is perhaps a less robust structure than in the human eye. Our study con-

firms that, at least in this eye, SD-OCT volumetric reconstruction appears to accurately capture the orientation of the border tissue relative to the sclera and Bruch's membrane.

A key finding of this study is the confirmation that SD-OCT is capable of detecting the prelaminar glial columns and the anterior surface of the lamina cribrosa. This suggests that SD-OCT may be useful for detecting morphologic changes in the prelaminar glial columns as well as displacement of the anterior lamina. Inoue et al.[26] recently identified the lamina cribrosa as highly reflective signal beneath the optic disc cup in horizontal SD-OCT B-scans acquired from glaucomatous or ocular hypertensive human eyes. Furthermore, the distance between the anterior and posterior borders of this signal was defined as the thickness of the lamina cribrosa. Laminar thickness measurements were found to have a high interobserver reproducibility and to be significantly correlated with visual field mean deviation.

Our comparisons between serial histology and SD-OCT in this monkey eye suggest that the detection of the lamina is not so straightforward. Within this SD-OCT volume, there was a distinction between the vertical striations, which most likely represent the prelaminar glial columns, and the interconnecting horizontal signal, which probably represents the horizontal laminar beams between the vertical septae. The anterior laminar signal is certainly more reflective in the SD-OCT horizontal B-scans presented by Inoue et al.,[26] than in the B-scans examined in the present study. Likewise, in our experience, the reflectivity of the anterior laminar surface is higher in human eyes than in monkey eyes. Laminar reflectivity appears to be further enhanced in highly myopic and glaucomatous eyes, which we assume is due to thinning of the prelaminar neural tissue. It is also important to note that, in humans, the central retinal trunk is located nasally whereas in the monkey, the trunk tends to be central (as in this study). If one assumes that laminar reflectivity is affected by the thickness of the prelaminar tissue, it follows that the most intense signal would be observed beneath the central, deepest part of the cup. Unfortunately, in the eye examined in this study, the signal from the
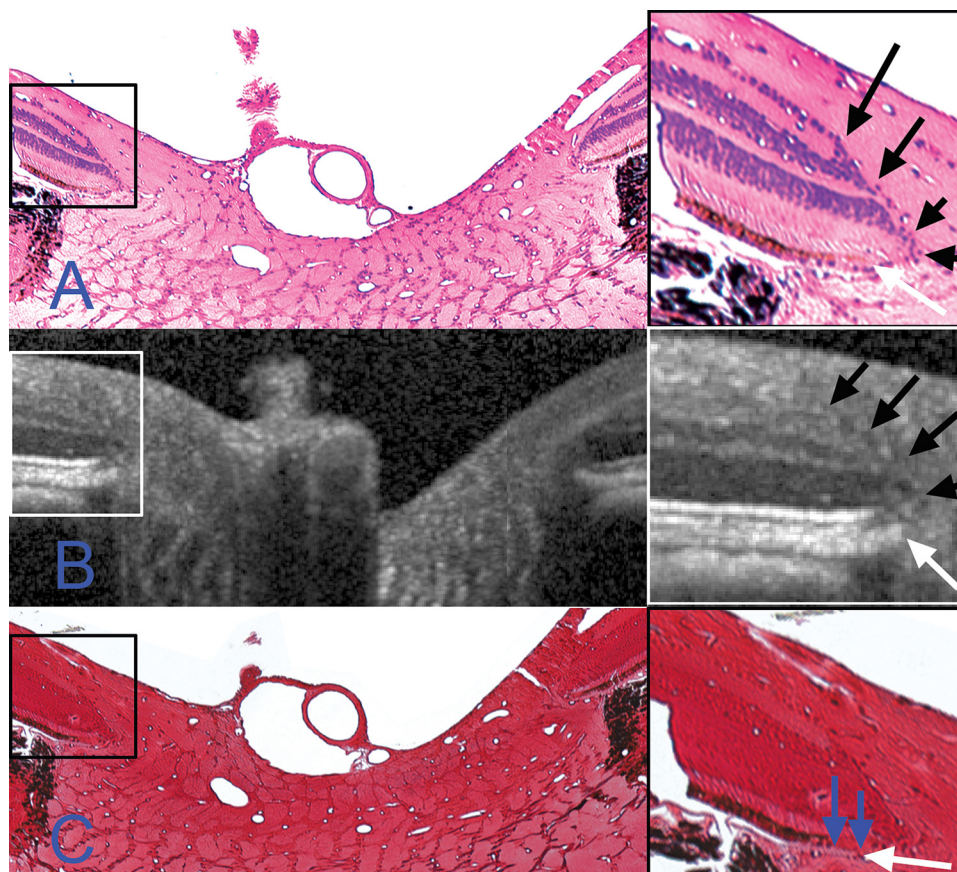
FIGURE 7. Identification of the neural canal opening. *Right*: Magnification of highlighted regions (*boxes, left*). Differences in anterior surface tilt between the B-scan and the histologic sections can be explained by the presence of retinal elevation/detachment and of a rip in the retina on the *left* side of the sections (both features cropped out of **A** and **C**). The retinal layers in (**A**) and (**C**) are as identified in Figure 5. (**A**) Section 257 (hematoxylin and eosin). The termination of Bruch's membrane (the neural canal opening) is highlighted with a *white arrow* in the magnified view. At this location, the retinal layers taper to a point (*black arrows*) at the photoreceptor layer, internal to the NCO. (**B**) Matched interpolated B-scan. The same relationship between the retinal layers (*black arrows*) and the termination of the retinal pigment epithelium/Bruch's membrane complex (*white arrow*), as was detected in (**A**), are seen in the magnified view. (**C**) Section 260 (Ponceau S). With this stain, the distinction between the termination of the retinal pigment epithelium and an extension of unpigmented Bruch's membrane (*blue arrows*) was clearly visible. Magnification: (**A, C**) ×10.

center of the lamina was obfuscated by fringe washout from the main vessel trunk.

It is also important to recognize that the ocular tissues of monkeys are more heavily pigmented than those of human eyes.[32] The heavy pigment on the surface of the anterior sclera (and indeed the peripheral lamina) of the eye examined in this study may have absorbed, rather than reflected, the incoming SD-OCT illumination, which may, in part, explain why there was no signal from the anterior scleral surface or from the peripheral lamina insertion.

In this eye, examined with a conventional 870-nm light source, the location of the posterior laminar surface was not apparent. In the B-scans examined in this study, the laminar signal appeared to fade with increasing depth through the ONH volume. We cannot be certain whether this decrease in reflectivity was due to the absence of horizontal laminar beams at the posterior laminar surface or because the posterior limit of tissue penetration was reached. For this reason, we advise exercising caution in trying to calculate in vivo laminar thickness by using SD-OCT. As Inoue et al.[26] have reported that their measurements of lamina thickness correlate with mean deviation in a cross-sectional cohort, the inference is that SD-OCT

can detect progressive laminar thinning in glaucoma. Although this suggestion is supported by a body of literature reporting that compression of the lamina occurs in the early, moderate, and severe stages of glaucomatous damage,[33–35] we have identified profound laminar thickening at the earliest stages of the neuropathy in a nonhuman primate model of glaucoma.[15] We hope that longitudinal in vivo SD-OCT ONH imaging will eventually assist in establishing the relationship between lamina morphology and stage of disease. Our confidence in identifying the posterior laminar surface may be increased with the adoption of a 1060-nm light source, which has increased axial penetration compared with the standard 870-nm light source as used in the imager (Spectralis; Heidelberg Engineering).[36–38] The deep ONH imaging capabilities of this alternative light source will be verified by repeating the current experiment with a prototype equipped with the alternative wavelength light source.

By elucidating the topographic location of the HE-stained sections with well-preserved retina, as depicted in Figure 4A, we identified a clear angular discrepancy between the histologic sections and the acquired B-scans in the superior third of the ONH. It is very unlikely that the microtome rotated
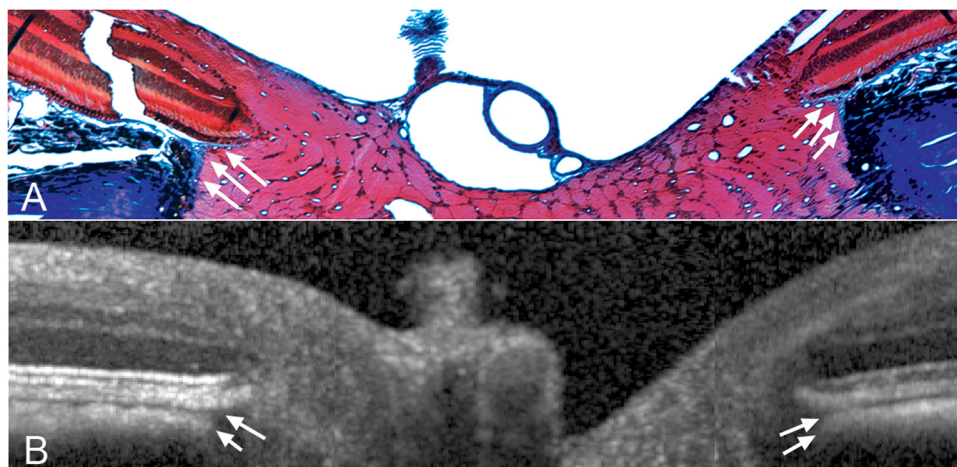
Figure 8. Detection of border tissue of Elschnig. (**A**) Section 258, with border tissue highlighted with *white arrows*. This histologic section was located immediately adjacent to the section shown in Figure 7. The border tissue of Elschnig was seen as a connective tissue strut (stained *blue*) connecting the anterior sclera to Bruch's membrane and enclosing the choroid. A more complete view of this section is shown in Figure 9. Masson trichrome; magnification, $\times 10$. (**B**, *white arrows*) The border tissue signal in the matched interpolated B-scan. SD-OCT appeared to accurately capture the orientation of the border tissue with an internally oblique configuration seen nasally (*left*) and an externally oblique configuration seen temporally (*right*).[28]

through successive sections to such an extent as to account for the observed discrepancy. The most likely explanation is that the retina in that region was elevated and curled upward within the block, resulting in a nonaligned portion of the retina contacting the microtome blade. Histologic sections in the lower two thirds of the nerve were fairly closely matched to the acquired B-scans, with only a 1° difference in the angle of rotation and the angle of incidence being perpendicular to the retinal surface. This observation suggests that the surface to-pography of the specimen was flatter and less variable in this region. The degree of retinal elevation in the ONH specimen may have been less pronounced, were a larger diameter ONH trephine selected. It is also possible that the perfusion fixation process contributed to the retinal elevation by causing expansion of the choroidal space. The presence of retinal elevation in the histologic sections explains the discrepancy observed in

the tilt of the anterior retinal surface in the histologic sections compared with the interpolated B-scans, particularly in Figure 7. There is also a substantial rip in the peripapillary retina present in the nasal half of the histologic sections shown in Figures 7, 8, and 9, which was likely to have further affected the degree of anterior surface tilt.

Our method of generating interpolated B-scans from the acquired SD-OCT volume represents a potentially important development in the visualization of ONH images. The matched interpolated B-scans in this report demonstrated minimal dim-inution in image quality compared with the acquired B-scans, despite the fairly wide variation in the angle of rotation and incidence. Greater diminution of image quality would have been observed if any of the interpolated B-scans had ap-proached a vertical orientation (perpendicular to the acquired B-scans). In the selected horizontal raster scan pattern, the
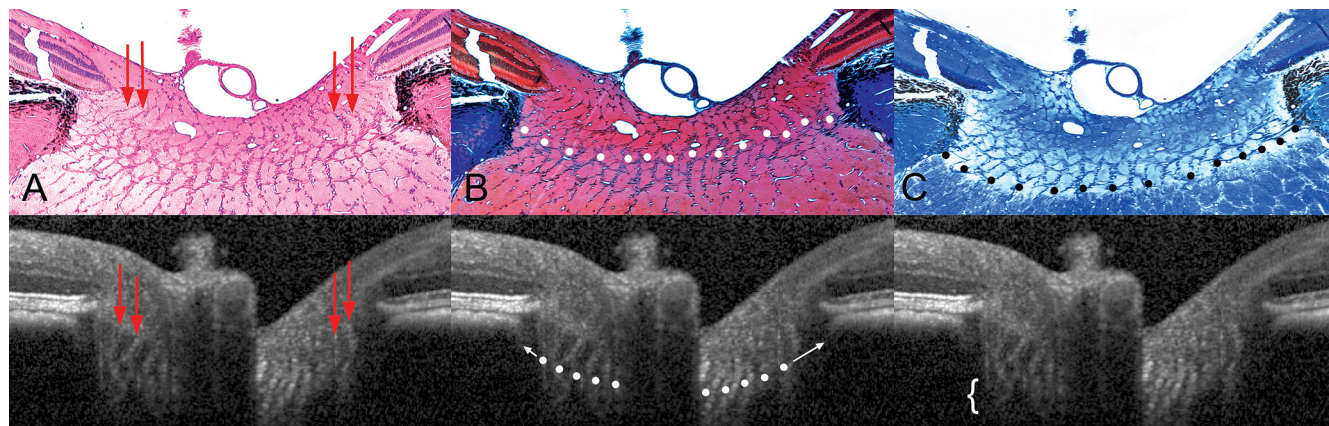
Figure 9. Detection of the lamina cribrosa. (**A**) Section 257. Prelaminar glial columns appear to correspond to vertical striations in the matched interpolated B-scan (*bottom*; marked with *red arrows*). Hematoxylin and eosin. (**B**) Section 258. The anterior lamina surface delineated with *white glyphs*. The peripheral insertion of the lamina is not clearly visible in the interpolated B-scan, although the approximate level of insertion could be ascertained by following the contour of the anterior laminar signal to the periphery of the neural canal (*white arrows*). Masson trichrome. (**C**) Section 256. Posterior lamina surface delineated with *black glyphs* in the histologic section. The posterior surface was not detectable in the matched interpolated B-scan, as the signal faded rather than coming to a discrete termination (region highlighted by a white bracket) Luxol fast blue stain. Magnification, $\times 10$.

x-axis contained 768 samples per 15°, whereas the *y*-axis contained 290 samples per 15°. The pixels generated were therefore not cubic but were "stretched" on the *y*-axis, with less density of data than that on the *x*-axis. A B-scan pattern with an equal sampling density in both axes would be necessary to minimize the diminution in image quality, regardless of the angle of rotation. Although it is theoretically possible to generate a 768 × 768, or indeed a 1536 × 1536, horizontal raster pattern scan with the Spectralis, achieving such a dense pattern would be limited in practical terms by the test's duration and by the memory constraints of the acquisition and viewing hardware and software.

The magnitude of the B-scans was adjusted by using a 1:1 scale to achieve the best approximate alignment between the interpolated B-scans and the serial histologic B-scans. Although an approximate horizontal alignment appears defensible, the B-scans appeared stretched in the vertical direction, with the cup and the anterior laminar surface seemingly deeper in the B-scan than in the matched histologic section. The SD-OCT volumes are transferred to our custom visualization software in a 1:1-μm scale, rather than in a 1:1-pixel scale. Although the *z*-axis scaling is fixed, the lateral magnification (*x*- and *y*-axis orientation) of the Spectralis is based on the optics of the human and not the macaque eye. The purpose of this study was to establish the histologic basis of SD-OCT signals deep within the ONH, rather than to achieve precise structural quantification. Although we are currently developing an algorithm for macaque-specific lateral magnitude scaling, that capability was beyond the scope of the present study. These scaling issues partly explain why the thicknesses of retinal layers (particularly the photoreceptor and the Bruch's membrane/retinal pigment epithelium) appeared much thicker in the interpolated B-scans than in the histologic sections. Undoubtedly, there is also an effect of differential tissue shrinkage, which was not corrected in the rescaling of the interpolated B-scans. Finally, the thicknesses in the deep retinal layers by SD-OCT are also likely to be influenced by the strength of reflected signal over distance, rather than just the thickness of the tissue of interest.

A major limitation of this work is that it was performed on a single monkey eye, which may mean that the results are not fully applicable to all human eyes. It is also important to recognize that the optic disc examined in this study had a very regular morphology, with a distinct clinical disc margin and no evidence of tilt or of peripapillary atrophy. Indeed these latter two features are far less prevalent in monkeys than in humans, and when present usually have a less exaggerated presentation than in the human eye. However, we believe that the merits of this study are such that the results are of relevance and interest. First, the morphology and histology of the monkey and human ONH are extremely similar and, as such, the characterization by SD-OCT is likely to be closely matched. By using a monkey eye, we were also able to perform SD-OCT imaging immediately before obtaining the tissue specimen by perfusion fixation. By using an anterior chamber manometer, we were able to establish the same level of IOP at the time of imaging and at the time of death. This kind of study cannot be replicated in a human eye.

This study provides histologic evidence that volumetric SD-OCT imaging of the ONH is capable of capturing ONH target structures, in particular the anterior laminar surface, which may prove useful in the detection of early changes in ocular hypertension and glaucoma.[15,39] Our novel method of generating interpolated SD-OCT B-scans at any angle of rotation or incidence will expand the clinical application of this technology in normal and glaucomatous human eyes.

References

1. Schuman JS, Hee MR, Arya AV, et al. Optical coherence tomography: a new tool for glaucoma diagnosis. *Curr Opin Ophthalmol.* 1995;6:89–95.
2. Nouri-Mahdavi K, Hoffman D, Tannenbaum DP, Law SK, Caprioli J. Identifying early glaucoma with optical coherence tomography. *Am J Ophthalmol.* 2004;137:228–235.
3. Sihota R, Sony P, Gupta V, Dada T, Singh R. Diagnostic capability of optical coherence tomography in evaluating the degree of glaucomatous retinal nerve fiber damage. *Invest Ophthalmol Vis Sci.* 2006;47:2006–2010.
4. Budenz DL, Michael A, Chang RT, McSoley J, Katz J. Sensitivity and specificity of the StratusOCT for perimetric glaucoma. *Ophthalmology.* 2005;112:3–9.
5. Anton A, Moreno-Montanes J, Blazquez F, Alvarez A, Martin B, Molina B. Usefulness of optical coherence tomography parameters of the optic disc and the retinal nerve fiber layer to differentiate glaucomatous, ocular hypertensive, and normal eyes. *J Glaucoma.* 2007;16:1–8.
6. Wollstein G, Schuman JS, Price LL, et al. Optical coherence tomography longitudinal evaluation of retinal nerve fiber layer thickness in glaucoma. *Arch Ophthalmol.* 2005;123:464–470.
7. Gaasterland D, Tanishima T, Kuwabara T. Axoplasmic flow during chronic experimental glaucoma: 1, light and electron microscopic studies of the monkey optic nervehead during development of glaucomatous cupping. *Invest Ophthalmol Vis Sci.* 1978;17:838–846.
8. Minckler DS, Bunt AH, Johanson GW. Orthograde and retrograde axoplasmic transport during acute ocular hypertension in the monkey. *Invest Ophthalmol Vis Sci.* 1977;16:426–441.
9. Quigley HA, Green WR. The histology of human glaucoma cupping and optic nerve damage: clinicopathologic correlation in 21 eyes. *Ophthalmology.* 1979;86:1803–1830.
10. Quigley HA, Addicks EM, Green WR, Maumenee AE. Optic nerve damage in human glaucoma, II: The site of injury and susceptibility to damage. *Arch Ophthalmol.* 1981;99:635–649.
11. Bellezza AJ, Rintalan CJ, Thompson HW, Downs JC, Hart RT, Burgoyne CF. Deformation of the lamina cribrosa and anterior scleral canal wall in early experimental glaucoma. *Invest Ophthalmol Vis Sci.* 2003;44:623–637.
12. Burgoyne CF, Downs JC, Bellezza AJ, Hart RT. Three-dimensional reconstruction of normal and early glaucoma monkey optic nerve head connective tissues. *Invest Ophthalmol Vis Sci.* 2004;45:4388–4399.
13. Roberts MD, Grau V, Grimm J, et al. Remodeling of the connective tissue microarchitecture of the lamina cribrosa in early experimental glaucoma. *Invest Ophthalmol Vis Sci.* 2009;50:681–690.
14. Yang H, Downs JC, Bellezza AJ, Thompson H, Burgoyne CF. 3-D histomorphometry of the normal and early glaucomatous monkey optic nerve head: Prelaminar Neural Tissues and Cupping. *Invest Ophthalmol Vis Sci.* 2007;48:5068–5084.
15. Yang H, Downs JC, Girkin C, et al. 3-D Histomorphometry of the normal and early glaucomatous monkey optic nerve head: lamina cribrosa and peripapillary scleral position and thickness. *Invest Ophthalmol Vis Sci.* 2007;48:4597–4607.
16. Downs JC, Yang H, Girkin C, et al. Three dimensional histomorphometry of the normal and early glaucomatous monkey optic nerve head: neural canal and subarachnoid space architecture. *Invest Ophthalmol Vis Sci.* 2007;48:3195–3208.
17. Chen TC, Cense B, Miller JW, et al. Histologic correlation of in vivo optical coherence tomography images of the human retina. *Am J Ophthalmol.* 2006;141:1165–1168.
18. Blumenthal EZ, Parikh RS, Pe'er J, et al. Retinal nerve fibre layer imaging compared with histological measurements in a human eye. *Eye.* 2009;23(1):171–175.

19. Toth CA, Birngruber R, Boppart SA, et al. Argon laser retinal lesions evaluated in vivo by optical coherence tomography. *Am J Ophthalmol.* 1997;123:188–198.

20. Toth CA, Narayan DG, Boppart SA, et al. A comparison of retinal morphology viewed by optical coherence tomography and by light microscopy. *Arch Ophthalmol.* 1997;115:1425–1428.

21. Anger EM, Unterhuber A, Hermann B, et al. Ultrahigh resolution optical coherence tomography of the monkey fovea. Identification of retinal sublayers by correlation with semithin histology sections. *Exp Eye Res.* 2004;78:1117–1125.

22. Abbott CJ, McBrien NA, Grunert U, Pianta MJ. Relationship of the optical coherence tomography signal to underlying retinal histology in the tree shrew (Tupaia belangeri). *Invest Ophthalmol Vis Sci.* 2009;50:414–423.

23. Ruggeri M, Wehbe H, Jiao S, et al. In vivo three-dimensional high-resolution imaging of rodent retina with spectral-domain optical coherence tomography. *Invest Ophthalmol Vis Sci.* 2007;48: 1808–1814.

24. Gloesmann M, Hermann B, Schubert C, Sattmann H, Ahnelt PK, Drexler W. Histologic correlation of pig retina radial stratification with ultrahigh-resolution optical coherence tomography. *Invest Ophthalmol Vis Sci.* 2003;44:1696–1703.

25. Kagemann L, Ishikawa H, Wollstein G, et al. Ultrahigh-resolution spectral domain optical coherence tomography imaging of the lamina cribrosa. *Ophthalmic Surg Lasers Imaging.* 2008;39:S126–S131.

26. Inoue R, Hangai M, Kotera Y, et al. Three-dimensional high-speed optical coherence tomography imaging of lamina cribrosa in glaucoma. *Ophthalmology.* 2009;116:214–222.

27. Burke D. A modification for the combined staining of cells and fibers in the nervous system. *Am J Med Technol.* 1968;34:667–670.

28. Strouthidis NG, Yang H, Downs JC, Burgoyne CF. Comparison of clinical and three-dimensional histomorphometric optic disc margin anatomy. *Invest Ophthalmol Vis Sci.* 2009;50:2165–2174.

29. Strouthidis NG, Yang H, Fortune B, Downs JC, Burgoyne CF. Detection of optic nerve head neural canal opening within histomorphometric and spectral domain optical coherence tomography data sets. *Invest Ophthalmol Vis Sci.* 2009;50:214–223.

30. Drexler W, Fujimoto JG. State-of-the-art retinal optical coherence tomography. *Prog Retin Eye Res.* 2008;27:45–88.

31. Anderson DR, Hoyt WF. Ultrastructure of intraorbital portion of human and monkey optic nerve. *Arch Ophthalmol.* 1969;82:506–530.

32. Marshall J, Hamilton AM, Bird AC. Histopathology of ruby and argon laser lesions in monkey and human retina: a comparative study. *Br J Ophthalmol.* 1975;59:610–630.

33. Emery JM, Landis D, Paton D, Boniuk M, Craig JM. The lamina cribrosa in normal and glaucomatous human eyes. *Trans Am Acad Ophthalmol Otolaryngol.* 1974;78:OP290–OP297.

34. Quigley HA, Hohman RM, Addicks EM, Massof RW, Green WR. Morphologic changes in the lamina cribrosa correlated with neural loss in open-angle glaucoma. *Am J Ophthalmol.* 1983;95:673–691.

35. Yan DB, Coloma FM, Metheetrairut A, Trope GE, Heathcote JG, Ethier CR. Deformation of the lamina cribrosa by elevated intraocular pressure. *Br J Ophthalmol.* 1994;78:643–648.

36. Povazay B, Bizheva K, Hermann B, et al. Enhanced visualization of choroidal vessels using ultrahigh resolution ophthalmic OCT at 1050 nm. *Opt Express.* 2003;11:1980–1986.

37. Povazay B, Hermann B, Unterhuber A, et al. Three-dimensional optical coherence tomography at 1050 nm versus 800 nm in retinal pathologies: enhanced performance and choroidal penetration in cataract patients. *J Biomed Opt.* 2007;12:041211.

38. Wang Y, Nelson J, Chen Z, Reiser B, Chuck R, Windeler R. Optimal wavelength for ultrahigh-resolution optical coherence tomography. *Opt Express.* 2003;11:1411–1417.

39. Yang H, Downs JC, Burgoyne CF. Physiologic intereye differences in monkey optic nerve head architecture and their relation to changes in early experimental glaucoma. *Invest Ophthalmol Vis Sci.* 2009;50:224–234.